Full paper

Visible-light induced Sustainable Water Treatment using Plasmo-semiconductor Nanogap bridge Array, PNA

*Emma Murphy,[a‡] Yunbo Liu,[b‡] Daniel Krueger,[c] Meghna Prasad,[a] Somin Eunice Lee,[*b,d] and Younggeun Park[*e]*

*Corresponding authors

Dr. Y. Park
Department of Mechanical Engineering, University of Michigan, Ann Arbor, MI 48109, USA

E-mail: ygpark@umich.edu

E. Murphy, M. Prasad

Department of Civil and Environmental Engineering, University of Michigan, Ann Arbor, MI 48109, USA

D. Krueger
Department of Chemical Engineering, University of Michigan, Ann Arbor, MI 48109, USA

Y. Liu, Prof. S. Lee
Department of Electrical Engineering and Computer Science, University of Michigan, Ann Arbor, MI 48109, USA

E-mail: sleee@umich.edu

Prof. S. E. Lee
Biointerfaces Institute, University of Michigan, University of Michigan, Ann Arbor, MI 48109, USA

Keywords: Interfacial antibacterial method, plasmo-semiconductor nanogap bridge, localized surface plasmon resonance (LSPR), bacteria, sustainable water treatment

Abstract: The development of sustainable methods for energy-intensive water treatment processes continues to be a challenging issue. Plasmonic-semiconductor nanoparticles, which absorb large amounts of sunlight in the visible range and convert it into chemical energy efficiently, can form the basis of a sustainable water treatment method. However, the potential uses of plasmonic semiconductor particles for water treatment have not been fully explored yet because of the limitations associated with the imbalance between light capture, charge transfer, and the required recycling steps for the particles themselves. Herein, we report on a significantly improved visible-light-induced water treatment method that uses a plasmo-semiconductor nanogap bridge array (PNA). As an arrangement of antenna-reactors, the PNA enables the balancing of the largely enhanced electromagnetic field in the plasmonic nanogap coupling region and optimal separation of charge carriers in the semiconductor. The simultaneous effects of visible-light absorption and charge transfer lead to the generation of a highly enhanced visible-light-induced OH radical (•OH). Consequently, we successfully demonstrated visible-light-induced 5-log N/No water disinfection and 100% chemical decomposition for sustainable water treatment. Owing to the large light absorption, charge carrier utilization, and array-oriented scalability, the PNA will be valuable in various sustainable energy and environmental applications.

1. Introduction

The utilization of solar energy driven by plasmonic nanostructures is attracting a great deal of attention for applications involving sustainable energy and environmental processes. In particular, the strong absorption/scattering stemming from localized surface plasmon resonance (LSPR) in plasmonic nanostructures can enable various sustainable solar-energy based technologies.

Recent studies have demonstrated the promising capabilities of such plasmonic nanostructures in LSPR-induced hot electrons, in which the nanostructures are useful for energy conversion and storage when combined with electron-accepting semiconductors such as plasmonic metallic-semiconductor nanostructures.[1-6] Hot electrons generated in semiconductor-plasmonic nanostructure (NS) composites have been shown to play a central role in increasing the efficiency of solar energy conversion because these materials allow for the tuning of the wavelength over a wide resonance in the visible to near-infrared (NIR) region by controlling the physical shape of the NSs [7, 8]. The underlying principle is mainly related to the surface plasmon energy transfer, in which the SP state of the metallic structure induces charge separation in the neighboring semiconductor, and this enables the solar energy conversion process. Plasmon-derived hot charge carriers in metallic nanostructures are transmitted to the semiconductor under visible light illumination [9-13]. As a result of the hole/electron charge carrier separation regardless of its bandgap energy, interfacial chemical transformation occurs. In accordance with this principle, the plasmonic metallic-semiconductor nanostructure holds great potential for future solar water remediation processes by allowing for the production of reactive oxygen species (ROS), e.g., hydroxyl radicals (OH), which can react unselectively and instantaneously with the surrounding toxic ingredients, such as undesirable organic compounds and biological species, and aid in their elimination [14]. Traditionally, the production of ROS requires high levels of energy consumption to achieve sufficient performance in conventional water treatment processes; however, the visible-light-induced production of ROS would allow for the transition to solar water treatment as a sustainable process.[15]

To date, there have been many efforts to explore energy transfer between plasmonics and semiconductor materials.[16-19] Most plasmonic-semiconductor studies in energy and environmental applications have been based on particles which have been synthesized using chemical synthesis techniques and overgrowth approaches. Although these particles showed a great control of the geometry, to achieve both of the large enhancement of electromagnetic field in the plasmonic structure and optimal separation of charge carriers in the semiconductor, precise design of interparticle distance and nanogap in the plasmonic-semiconductor structure have to be addressed. In addition, unlike gas-phase reaction which has been mostly explored, water treatment using the plasmonic semiconductor nanoparticles necessitates post-processing to can recycle nanoparticles within the mixture solution after the photoreaction.

Despite the growing interest in this topic, the possibility of using plasmonic metallic semiconductor nanostructures in water treatment applications has not been explored. To make such a sustainable water treatment process feasible, a comprehensive approach to engineering geometry of plasmonic semiconductor structure that combines the solar energy capture, hot-electron generation, and energy transfer phases in an array type within large-area substrates will be required.

In this study, we report significantly enhanced visible-light-induced water treatment effects resulting from the use of an array of plasmo-semiconductor nanogap bridge array (PNA) (**Figure 1**). We systematically characterized the optical properties of the PNA, which showed strong plasmonic coupling in the nanogap and thereby increased visible-light absorption. In addition, we demonstrated enhanced plasmon resonance energy transfer (PRET) in the multi-dimensional metal-

semiconductor structure resulting from the plasmonic nanogap of the TiO_2 layer. Finally, we showed that greatly enhanced generation of OH radicals results in significant improvements in bacterial inactivation by the multidimensional metal-semiconductor nanostructure array.

2. Results and Discussions

For optimal photocatalytic reaction, the metallic-semiconductor nano structures should be designed not only to maximize local field enhancement at the catalytic interface but also to optimize transfer of charge carriers where charge separation and surface reaction occurs. The metallic-semiconductor nanostructure array for this study were designed to exploit this type of coupling.

2.1. Multidimensional plasmonic semiconductor array fabrication and characterization

In the PNA geometry, the coupled AuNS array induces a highly focused local electromagnetic (*E*)-field. The hot electrons in the plasmonic nanostructure to the nanogap of TiO_2 generate highly energetic charge carriers' separation. The separated charges then diffuse into the interface between the PNA and H_2O[7, 8, 10, 20, 21]. In this geometry, the plasmonic nanogap of TiO_2 determines plasmonic coupling between top/bottom AuNS and the charge separation.

We constructed the PNA in the multidimensional arrays of AuNS by combining thermal dewetting and evaporating of the nanostructure (**Figure 2**). This approach enabled control of the plasmonic nanogap ($\delta_{nanogap}$) between the first and second AuNS array layers due to TiO_2 layers with thickness variation from 1 to 30 nm (**Figure 2a** and **Figure S1**). To ensure the crystallinity of the TiO_2 layer, a thermal treatment step then followed.[22] Subsequently, we characterized the fabricated structure. Firstly, the fabricated PNA ($\delta_{nanogap}$ = 8) has a hemispherical bump structure array within ~ 20 nm height profile as determined by atomic force microscopy (AFM) (**Figure 2b**). The scanning electron microscopy (SEM) images show that the AuNS array consisted of thin asymmetric spheres with an average interparticle distance of ~ 45 nm (<~20% standard deviation) and uniform distribution in the size (d_{PNA} = 40 nm ± 25%) with high density (ρ_{PNA} = ~ 880 AuNSs/μm^2) (**Figure 2c**). After adding the TiO_2 layer as a plasmonic nanogap on the first AuNS array, the second (top) AuNS array were prepared, sequentially. The SEM images of TiO_2/AuNS and PNA ($\delta_{nanogap}$ = 8 nm) from the top-view reveals similar distribution of that from the first AuNS array. The energy-dispersive X-ray spectroscopy (EDS) elemental analysis of the PNA samples reveals identifiable components of the layered nanostructures. The acquired EDS spectrum from the PNA on a glass substrate clearly shows Au, Ti, and O elements including glass elements (Si, Na, and Mg) (**Figure 2d**). The counts of Ti increase with $\delta_{nanogap}$ from 1 to 30 nm. The cross-sectional SEM images different $\delta_{nanogap}$ shows that the thickness of TiO_2 nanogap layer increased with $\delta_{nanogap}$ (**Figure 2e** and **Figure S2**). We plotted the measured $\delta_{nanogap}$ in the PNA samples as a function

of the deposition condition used in the fabrication process. The data show that on average deposition rate results in 0.1 nm per min of TiO_2. The measured $\delta_{nanogap}$ shows a linear trend with the process condition while the AuNSs shows uniform sizes. The top and bottom AuNS arrays showed consistent hemispherical shape, size (40 nm ± 13%), and interparticle distance (45 nm ± 11%). The diameter of AuNS on the top layer shows minimal change as a function of the $\delta_{nanogap}$ between 1 and 30 nm. The AuNS particle size distribution analysis also showed a minimal change with the $\delta_{nanogap}$ variation (**Figure 2f**). These results support the successful fabrication of a PNA structure exhibiting high density and uniform size distribution.

2.2. Characterization of the field enhancement and optical properties

With the constructed PNA structures, we characterized the optical properties (**Figure 3**). First, we estimated the local electric (*E*)-field distribution and its enhancement (= $|E_n/E_0|^2$, where E_0 is the base *E*-field intensity and E_n is the enhanced electric field intensity) around the representative PNA structure using a finite element analysis (FEA) (see Supplementary information) (**Figure 3a,b**). Under visible-light illumination (λ = 650 nm), the PNA showed a strong *E*-field focusing in the nanogap owing to the strong plasmonic coupling inducing a power transfer. On the other hand, the AuNS and TiO_2/AuNS revealed a focused *E*-field around the edge of the AuNS. With the FEA results, we measured the optical properties of AuNS, TiO_2/AuNS, and PNA (**Figure 3c**). First, the AuNS array resulted in a resonance peak at 580 nm. Then, layering the TiO_2 nanolayer (δ_{TiO2} = 8 nm) on the AuNS array led a redshift owing to the higher reflective index of TiO_2. The nanogap of TiO_2 layer does

not reveal any optical extinction in the visible range. The optical properties of the PNA structure indicate that the nanogap of TiO_2 layer induces nano plasmonic coupling and highly enhanced visible-light absorption. To explore the effect of the plasmonic nanogap of TiO_2 nanolayer on a channel for plasmon-pathway, we further characterized the optical properties of the PNA structure as a function of the $\delta_{nanogap}$ from 1 to 30 nm (**Figure 3d**). The LSPR peak shifted from 750 to 530 nm with the $\delta_{nanogap}$. The highest extinction occurred around $\delta_{nanogap}$ 8 nm. Furthermore, we compared maximum intensity of scattering and extinction as a function of $\delta_{nanogap}$ (**Figure 3e**). We used a dark-field microscope to acquire scattering spectra (see Methods). The scattering intensity (I_{scat}) decreased with $\delta_{nanogap}$ as we observed in the FEA results. Meanwhile, the highest extinction intensity (I_{ext}) is shown around $\delta_{nanogap}$ = 8 nm which is comparable to the charge diffusion distance in the TiO_2 structure.[14, 23] The plasmonic nanogap of TiO_2 functions as a channel that induces plasmon decay, forming energetic charge carriers (*e* - *h* pairs). The TiO_2 nanolayer between the coupled AuNS arrays leads to the generation of hole-electron pairs and it becomes a critical plasmon-pathway.

2.3. Hydroxyl radical generation

The strong visible-light absorbance of the PNA is expected to result in a rapid charge transfer to the TiO_2 [7, 8, 10, 20, 21]. Charge separation in the TiO_2 layer leads to surface reactions that generate $^{\bullet}OH$ at the interface of the AuNS, TiO_2, and H_2O (**Figure 4**). In plasmonic-semiconductor nanostructures, when LSPR exists in the AuNS under light illumination, through hot electronic injection, energetic and ballistic electrons generated inside the AuNS are injected into the conduction band of the TiO_2 layer. In this interfacial electron transition, electrons in the metal are directly

excited to a level in the semiconductor, typically from the Fermi level of the AuNS to the conduction band of the TiO_2. The pair of electric charges thus separate, namely a negative one in the TiO_2 conduction band and a positive one in the AuNS, and have electrochemical energy, which can be further converted into chemical energy (e.g., hydroxyl radicals, $^{\bullet}OH$) for water treatment (**Figure 4a**).

To confirm $^{\bullet}OH$ generation under visible light illumination (**Figure S3**), we performed a photocatalytic $^{\bullet}OH$ generation test and we adopted a chemical transformation reaction of terephthalic acid (TA) to 2-hydroxyterephthalic acid (TAOH) (**Figure 4b**). This reaction was used to estimate $^{\bullet}OH$ generation. The reaction between single OH radicals and TA molecules produced single fluorescence TAOH molecules (excitation wavelength (λ_{ext}) = 450 nm and emitting wavelength (λ_{emit}) = 475 nm) (**see Method section**).[24] In this test, the PNA was integrated into a polydimethylsiloxane (PDMS) microfluidic chamber (see **Method section**). Under visible-light illumination[18, 25, 26] (light intensities, I = 200 mW/cm^2) at TA concentration (C_{TA}) = 100 μM, we compared OH radical generation from PNA (R_{OH_ATA}) with that from AuNS and TiO_2/AuNS, individually. The R_{OH_ATA} (= 5.6 × 10^{-10} M/ min) shows faster OH radical generation than that R_{OH_A} (= 2.2 × 10^{-10} M/min) and R_{OH_TA} (= 0.7 × 10^{-10} M/min). The combined effect of the plasmonic coupling and the charge separation in the plasmonic nanogap of TiO_2 layer led to the enhanced OH radical generation performance. Under dark condition, we did not observe any noticeable OH radical generation from any of the samples.

2.4. Visible light-induced photocatalytic performance

For the quantification of OH radical, a high pH solution (pH = ~ 13) was used to dissolve the TA due to low solubility (0.0015 g/100 mL at 20 °C). This high pH condition is also desirable to enhance conversion of the photocatalytic reaction on TiO_2 surface,[27, 28] however, the pH condition limits the practical water treatment model to pH = 5-9[29]. In this consideration, we continued tests of a methylene blue (MB) decomposition (**see Method section**). First, we confirmed visible light effect on the conversion of MB degradation (**Figure 4c**). In this test, we integrated the PNA into a polydimethylsiloxane (PDMS) microfluidic chamber (**Figure S4**). The conversion of MB degradation, *Conv* (= $(C_{MB0}-C_{MB})/C_{MB0}$, where C_{MB0} and C_{MB} are the MB concentrations before and after the reaction, respectively) revealed sensitive increases with the I_{light} from 50 to 200 mW/cm^2 in PNA compared to those in TiO_2/AuNS and TiO_2, which showed less sensitivity at the same condition. In particular, PNA structure with $\delta_{nanogap}$ = 8 nm led to *Conv* of 99%, meanwhile 56% and 30% were obtained in TiO_2/AuNS and TiO_2, respectively, at I = 200 mW/cm^2. Furthermore, to confirm the visible light-induced photocatalytic activity of the PNA, we plotted the *Conv* as a function of incident wavelengths between 400 and 700 nm (**Figure 4d**). Specifically, at λ =650 nm, we observed the maximum *Conv* (= ~ 90%) in PNA, while TiO_2/AuNS and TiO_2 resulted in *Conv* of ~ 70 and ~ 20 % at λ = 600 and 400 nm, respectively. This spectrum dependence of MB degradation is consistent with the characterized absorption spectrum in figure 3.

When the plasmonic coupling solely contributed the photocatalytic reaction, narrower nanogap will result in higher rate of $^{\bullet}$OH generation. However, since charge separation occurs in the TiO_2 nanogap, simultaneously, a dimension of TiO_2 nanogap enabling efficient diffusion of the separated charges must be considered to maximize $^{\bullet}$OH. The separated charge carrier transfer is involved in the charge-carrier diffusion length. In this consideration, we estimated the TiO_2 nanolayer effect on the MB decomposition by varying the $\delta_{nanogap}$ from 1 to 30 nm (**Figure 4e**). The highest *Conv* of ~ 98% at $\delta_{nanogap}$ = 8 nm occurred after 60 min reaction. When $\delta_{nanogap}$ increased to 30 nm, ξ gradually decreased to ~ 51%. However, when $\delta_{nanogap}$ was thin (= 1 nm), we observed *Conv* = 75%, which was lower than that with $\delta_{nanogap}$ = 8 nm. In the below 10 nm range, a discrepancy between the plasmonic nanogap of TiO_2 layer and the minority charge diffusion length occurred [23]. Plasmonic coupling was stronger in the thin TiO_2 layer, but the charge diffusion cannot be maximized due to the low charge separation. On the other hand, in the case of thick $\delta_{nanogap}$ (> 8 nm), although a wider plasmonic nanogap of TiO_2 layer induced larger charge diffusion, it lowered the plasmonic coupling. Accordingly, to maximize the combined effects of the plasmonic nanogap and the charge diffusion in the TiO_2 nanolayer between two AuNS arrays, we optimized the TiO_2 layer thickness ($\delta_{nanogap}$ = 8 nm) for simultaneous light harvesting and OH radical generation under visible light. The *E*-field in PNA at $\delta_{nanogap}$ = ~ 8 nm resulted in a rapid charge separation comparing the AuNS and TiO_2/AuNS (**Figure S5**) as well as a faster photocatalytic reaction rate.

2.3. Visible induced bacteria inactivation

We turned to visible light induced inactivation of bacterial particles in water based on the mechanism of photocatalytic performance enhanced by PNA (**Figure 5**). The visible induced • OH generation from PNA expected to damage the membrane of bacterial particles in water (**Figure 5a**). The tests were performed in the PNA integrated microfluidic reactor to enable straightforward setup and operation for a potential solar panel design (**see Method section**). In this test, as a representative water pathogen model, we used *Escherichia coli* (*E. coli*) K-12 (~5×10^6 CFU) in a tap water-based medium (Washtenaw County, MI USA) (**see Method section**). First, to confirm the photocatalytic inactivation, we characterized the *E. coli* morphology by obtaining SEM images (**Figure 5b**). In PNA with $\delta_{nanogap}$ = 8 nm, the images of the treated *E. coli* sample under light illumination (I = 200 mW/cm^2) for 90 min, we observed membrane damage in which pores were formed by OH radicals. This inactivation of treated *E. coli* in PNA was quantified by estimating - log$N$/logN_0 (N and N_0 are the *E. coli* populations before and after the treatment, respectively), and we compared it with them in control, AuNS array, and TiO_2/AuNS array (**Figure 5c**). PNA was the most effective for inactivating *E. coli*. PNA was the most broadly effective material, able to achieve a 6-log inactivation of *E. coli*, and a 4.7 and 4.1- log inactivation in 60 min illumination. The -log$N$/logN_0 value of AuNS array indicates that photothermal effect is involved in the inactivation of *E. coli*.

In the PNA structure, if the photothermal effect on the *E. coli* inactivation is significant, narrower nanogap leading to larger photothermal effect owing to focused *E*-field will result in higher performance in *E. coli* inactivation. On the other hand, if

the photocatalytic effect is dominant, the inaction performance will follow the trends of OH radical generation as a function of $\delta_{nanogap}$. To confirm this, we tested the effect of nanogap thickness and I on the inactivation performance by estimating - log$N$/ logN_0 by varying the $\delta_{nanogap}$ from 1 to 30 nm (**Figure 5d**). The lowest log$N$/logN_0 of -5 at $\delta_{nanogap}$ = 8 nm under the same light illumination condition was observed. This *E. coli* deactivation trends is similar to that of MB decomposition. This result clearly indicates that the combined mechanism of larger light absorption and charge transfer led to such high inactivation.

Considering the optofluidic performance, to investigate retention time effect, we further evaluated the *E. coli* inactivation performance as a function of flow rate (Q) ranging from 1 to 20 ml/min (**Figure 5e**). In this optofluidic panel test, this range of flow rates was decided according to the average volume of greywater production per day in a single family household in the USA[30, 31]. In general, μ_D decrease with Q, and the highest μ_D was observed at $\delta_{nanogap}$ = 8 nm and Q = 1 ml/min. Taken together, these results successfully demonstrate visible-light-induced 5-log N/No water disinfection and 100% chemical decomposition for the sustainable water treatment.

3. Conclusions

In this study, we studied highly sustainable solar water inactivation with the multidimensional PNA structure. The multidimensional PNA allowed significantly enhanced visible-light focusing and rapid charge separation for rapid OH radical generation. In this multidimensional

geometric arrangement, the TiO_2 nanolayer between the two layers of the AuNS array played the critical roles of i) a plasmonic nanogap enhancing local electric field, ii) a diffusion channel for separated charge carriers, and iii) an active sites for catalytic generation of OH radicals. Through the geometric arrangement of the TiO_2 nanolayer in the plasmonic coupling, we successfully demonstrated that optimizing the charge carrier length in the plasmonic nanogap of TiO_2 layer led to highly enhanced the *E. coli* inactivation. The PNA potentially targets an optofluidic panel for solar water treatment by introducing scale-up method. Similar to a conventional solar panel, which converts sunlight into electrical energy, the thin optofluidic panel with PNA integration can be potentially installed on the exteriors of houses or buildings. The PNA will be integrated into the optofluidic platform, and, under sunlight illumination, the flow of the contaminated water on the metal semiconductor structure enables recycling of the treated water. We expect that the integrated optofluidic panel will be widely used to treat low-contaminated water (e.g., greywater) from buildings and houses owing to its energy sustainability, set-up flexibility, and scalability (**Figure S6**).

4. Experimental Section

Materials: 2-hydroxyterephthalic acid (TAOH), terephthalic acid (TA), Methylene blue (MB), Sodium hydroxide (NaOH) were purchased from Sigma Aldrich Inc.. Polydimethylsiloxane (PDMS) were purchased from Dow chemicals Inc.. The high-purity water used was distilled, deionized and then purified with the Milli-Q system (Nippon Millipore Co., Tokyo).

PNA fabrication: After Au deposition on a clean SiO_2 substrate (4inch wafer), we performed a dewetting step at 450^{o}C for 10 min using lamp-heated Rapid Thermal Process (RTP) (Jetfirst RTP 150) (see Supplementary information). After confirming the uniform Au nanostructures (AuNS) array, we layered TiO_2 nanolayer using E-beam evaporation (Angstrom Engineering Evovac Evaporator) on top of the AuNS. To ensure crystallinity of the TiO_2 layer[22, 32], we annealed the sample at 400^{o}C for 1 hr. We next constructed another AuNS layer on top of the TiO_2/AuNS at the same condition as for the first the AuNS layer.

Characterization of morphologies and optical properties: Morphologies of the PNA samples were analysed by SEM images, Image J, and AFM (see Supplementary information). The optical properties of PNA was characterized by a dark-field microscope with a dark field condenser lens (NA = 1.45, MBL12000, Nikon). Global optical properties of the samples were measured by a UV-Vis spectrometer (Agilent 8453).

Construction of the integrated optofluidic device: We designed an optofluidic reactor consisting of an optical window and 5×5 micro pillar arrays in the reaction chamber area (see Supplementary information). We fabricated the optofluidic reactor according to the PDMS based soft-lithography process.

Quantification of hydroxyl radicals: We employed a stand scavenger reaction (see Supplementary information). Chemical transformation of terephthalic acid (TA) with the generated OH radicals results in formation of 2-hydroxyterephthalic acid (TAOH) (see Supplementary information). By analysing the TAOH which is fluorescence

molecules in treated sample, the generated OH radical quantified. The TAOH analyses were performed using a microplate reader (BioTek, Inc.).

Visible light induced photocatalytic reaction: We estimated the photocatalytic activity of the system in the optofluidic reactor under visible light illumination (Dolan-Jenner Fiber-Lite 180 with a 150W, 21 V halogen (EKE) lamp) (see Supplementary information). The flow rate of the solution into an optofluidic reactor was controlled by using a syringe pump (Cole Palmer, EW-74900-00). The treated sample solution was analysed using a UV-vis absorbance spectrometer (Agilent Technologies, Inc.) and microplate reader.

***E. coli* inactivation test:** The cultured bacteria were added to 10 mL of Luria-Bertani (LB) broth and incubated it (see Supplementary information). Using an OD meter, a portion of the solution containing the bacteria was diluted to $\sim 5 \times 10^6$ CFU/mL with tap water. Under visible light illumination, we flowed the prepared *E. coli* sample in the reactor and collected the treated *E. coli* solution through the outlet of the optofluidic reactor to a microtube. We then characterized and quantified the treated *E. coli* samples: i) after the dehydration of the treated *E. coli*, we obtained SEM images, and ii) we quantified the number of inactivated *E. coli* using a standard spread-plate counting method.

Model local electric (E) field distribution: We used finite element analysis (FEA, COMSOL Multiphysics software) (see Supplementary information). To characterize *E*-field around PNS, AuNS, and TiO_2/AuNS. Based on the obtained SEM images, we

defined representative geometry of PNA (Au diameter = 40 nm, Au thickness = 20 nm, and interparticle distance = 40 nm) and thickness of TiO_2 layer was changed from 1 to 30 nm. We estimated *E*-field and energy around the PNS, AuNS, and TiO_2/AuNS as a function of wavelength and direction of the incident light.

Supporting Information

Supporting Information is available from the Wiley Online Library or from the author.

Acknowledgement

This research was supported by academic research fund (U052481) and Mcubed (U064088) at the University of Michigan, the National Science Foundation (ECE 1454188), and the Air Force Office of Scientific Research (AFOSR FA9550-16-1-0272).

Conflict of Interest

The authors declare no conflict of interest.

References

1. César Clavero, *Nature Photonics* **2014,** *8* (2), 95-103.

2. Carl Hägglund; Gabriel Zeltzer; Ricardo Ruiz; Isabell Thomann; Han-Bo-Ram Lee; Mark L Brongersma; Stacey F Bent, *Nano letters* **2013,** *13* (7), 3352-3357.

3. Keisuke Kimura; Shin-ichi Naya; Yasuaki Jin-nouchi; Hiroaki Tada, *The Journal of Physical Chemistry C* **2012,** *116* (12), 7111-7117.

4. M Murdoch; GIN Waterhouse; MA Nadeem; JB Metson; MA Keane; RF Howe; J Llorca; H Idriss, *Nature Chemistry* **2011,** *3* (6), 489.

5. Jacqueline B Priebe; Michael Karnahl; Henrik Junge; Matthias Beller; Dirk Hollmann; Angelika Brückner, *Angewandte Chemie International Edition* **2013,** *52* (43), 11420-11424.

6. Ying-Chih Pu; Gongming Wang; Kao-Der Chang; Yichuan Ling; Yin-Kai Lin; Bob C Fitzmorris; Chia-Ming Liu; Xihong Lu; Yexiang Tong; Jin Z Zhang, *Nano letters* **2013,** *13* (8), 3817-3823.

7. Phillip Christopher; Hongliang Xin; Suljo Linic, *Nature chemistry* **2011,** *3* (6), 467-472.

8. Phillip Christopher; Hongliang Xin; Andiappan Marimuthu; Suljo Linic, *Nature materials* **2012,** *11* (12), 1044.

9. William R Erwin; Holly F Zarick; Eric M Talbert; Rizia Bardhan, *Energy & Environmental Science* **2016,** *9* (5), 1577-1601.

10. Jiangtian Li; Scott K. Cushing; Fanke Meng; Tess R. Senty; Alan D. Bristow; Nianqiang Wu, *Nat Photon* **2015,** *9* (9), 601-607.

11. Shaunak Mukherjee; Linan Zhou; Amanda M. Goodman; Nicolas Large; Ciceron Ayala-Orozco; Yu Zhang; Peter Nordlander; Naomi J. Halas, *Journal of the American Chemical Society* **2014,** *136* (1), 64-67. DOI 10.1021/ja411017b.

12. Alejandro Manjavacas; Jun G. Liu; Vikram Kulkarni; Peter Nordlander, *ACS Nano* **2014,** *8* (8), 7630-7638. DOI 10.1021/nn502445f.

13. Kaifeng Wu; Jinquan Chen; James R McBride; Tianquan Lian, *Science* **2015,** *349* (6248), 632-635.

14. Rod G Zika; William J Cooper, *Photochemistry of environmental aquatic systems*. ACS Publications: **1987**.

15. Brenna C. Hodges; Ezra L. Cates; Jae-Hong Kim, *Nature Nanotechnology* **2018,** *13* (8), 642-650. DOI 10.1038/s41565-018-0216-x.

16. Sarah Griffin; Nicholas P. Montoni; Guoliang Li; Patrick J. Straney; Jill E. Millstone; David J. Masiello; Jon P. Camden, *The Journal of Physical Chemistry Letters* **2016,** *7* (19), 3825-3832. DOI 10.1021/acs.jpclett.6b01878.

17. Ana M. Brown; Ravishankar Sundararaman; Prineha Narang; William A. Goddard; Harry A. Atwater, *ACS Nano* **2016,** *10* (1), 957-966. DOI 10.1021/acsnano.5b06199.

18. Calvin Boerigter; Robert Campana; Matthew Morabito; Suljo Linic, *Nature Communications* **2016,** *7*, 10545. DOI 10.1038/ncomms10545.

19. Marco Bernardi; Jamal Mustafa; Jeffrey B. Neaton; Steven G. Louie, *Nature Communications* **2015,** *6*, 7044. DOI 10.1038/ncomms8044.

20. M. Bernardi; M. Palummo; J. C. Grossman, *Nano Letters* **2013,** *13* (8), 3664-3670. DOI Doi 10.1021/Nl401544y.

21. Stefan A Maier; Harry A Atwater, *Journal of Applied Physics* **2005,** *98* (1), 011101.

22. Kazuya Nakata; Akira Fujishima, *Journal of Photochemistry and Photobiology C: Photochemistry Reviews* **2012,** *13* (3), 169-189. DOI https://doi.org/10.1016/j.jphotochemrev.2012.06.001.

23. S. Girish Kumar; L. Gomathi Devi, *The Journal of Physical Chemistry A* **2011,** *115* (46), 13211-13241. DOI 10.1021/jp204364a.

24. Y. Nakabayashi; Y. Nosaka, *Physical chemistry chemical physics : PCCP* **2015,** *17* (45), 30570-6. DOI 10.1039/c5cp04531b.

25. Calvin Boerigter; Umar Aslam; Suljo Linic, *ACS Nano* **2016,** *10* (6), 6108-6115. DOI 10.1021/acsnano.6b01846.

26. Suljo Linic; Umar Aslam; Calvin Boerigter; Matthew Morabito, *Nature Materials* **2015,** *14*, 567. DOI 10.1038/nmat4281.

27. Yukihiro Nakabayashi; Yoshio Nosaka, *Physical Chemistry Chemical Physics* **2015,** *17* (45), 30570-30576. DOI 10.1039/C5CP04531B.

28. Jenny Schneider; Masaya Matsuoka; Masato Takeuchi; Jinlong Zhang; Yu Horiuchi; Masakazu Anpo; Detlef W. Bahnemann, *Chemical Reviews* **2014,** *114* (19), 9919-9986. DOI 10.1021/cr5001892.

29. Michael Oteng-Peprah; Mike Agbesi Acheampong; Nanne K. deVries, *Water Air Soil Pollut* **2018,** *229* (8), 255-255. DOI 10.1007/s11270-018-3909-8.

30. Maria Paz Gutierrez; Luke P Lee, *Science* **2013,** *341* (6143), 247-248.

31. Odeh R Al-Jayyousi, *Desalination* **2003,** *156* (1), 181-192.

32. Keiichi Tanaka; Mario F. V. Capule; Teruaki Hisanaga, *Chemical Physics Letters* **1991,** *187* (1), 73-76. DOI https://doi.org/10.1016/0009-2614(91)90486-S.

Figures and Captions

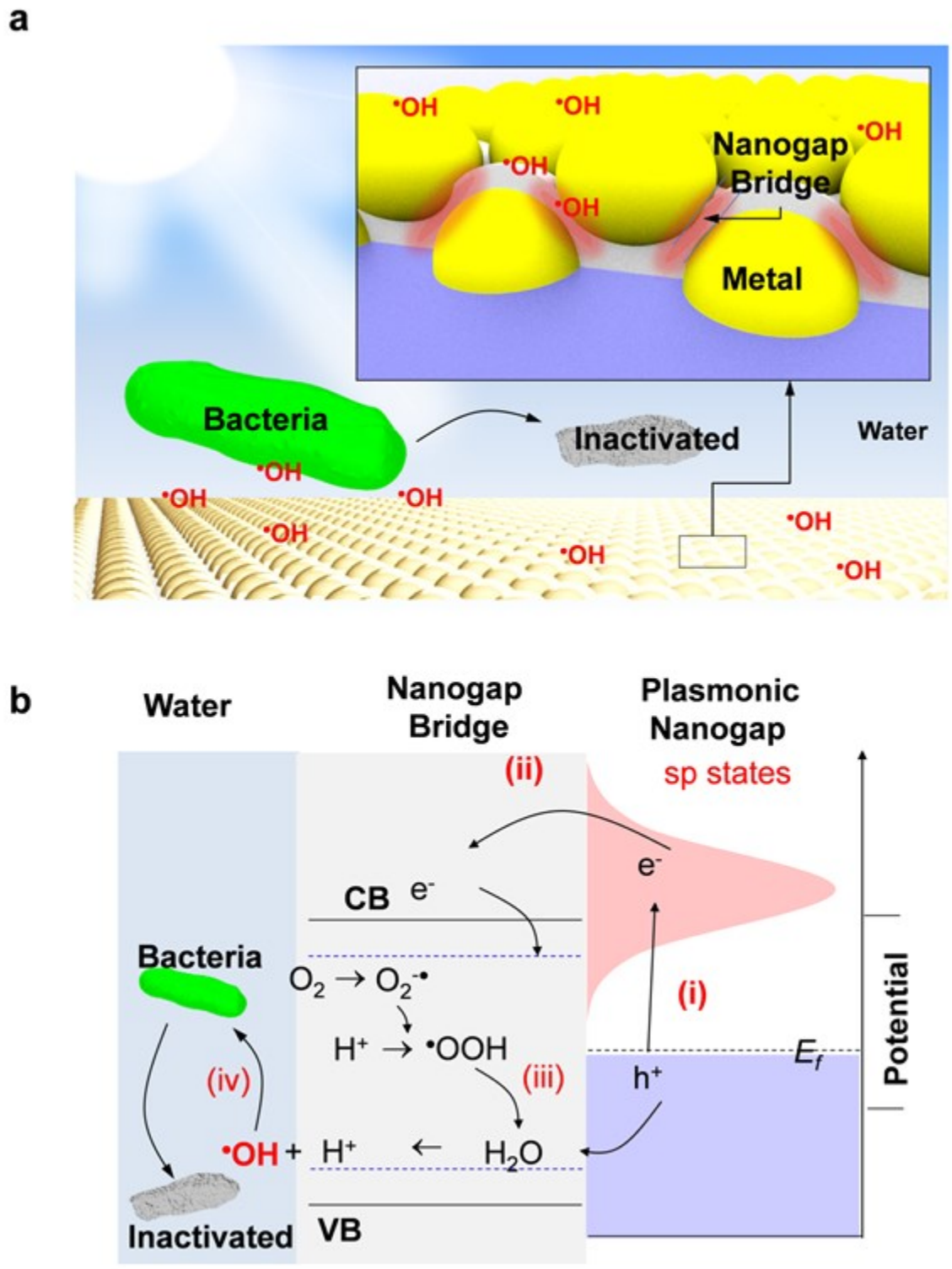

Figure 1. Visible light induced water treatment with plasmo-semiconductor nanogap bridge, PNA. (a) Schematic that shows that plasmonic nanogap bridged by semiconductor nanolayer with interacting bacteria in water through visible-light photocatalytic reactive oxygen species (ROS) generation. The nanogap plays roles in visible light focusing and charge separation to maximize the ROS generation. (b) Mechanism of nanogap assisted plasmonic resonance energy transfer (PRET) with energy levels on charge separation. Blue lines indicate the energy level for surface ROS (ex. OH radicals) generation. This mechanism involves following steps; (i) Nanogap assisted SP state which is excited from electrons around the Fermi level (E_f) of the metallic structure, (ii) the transfer of the excited hot electrons to a neighboring TiO_2 nanostructure, (iii) charge separation between valance band (VB) and conduction band (CB) induced ROS generation, and (iv) Bacteria inactivation by the the generated ROS.

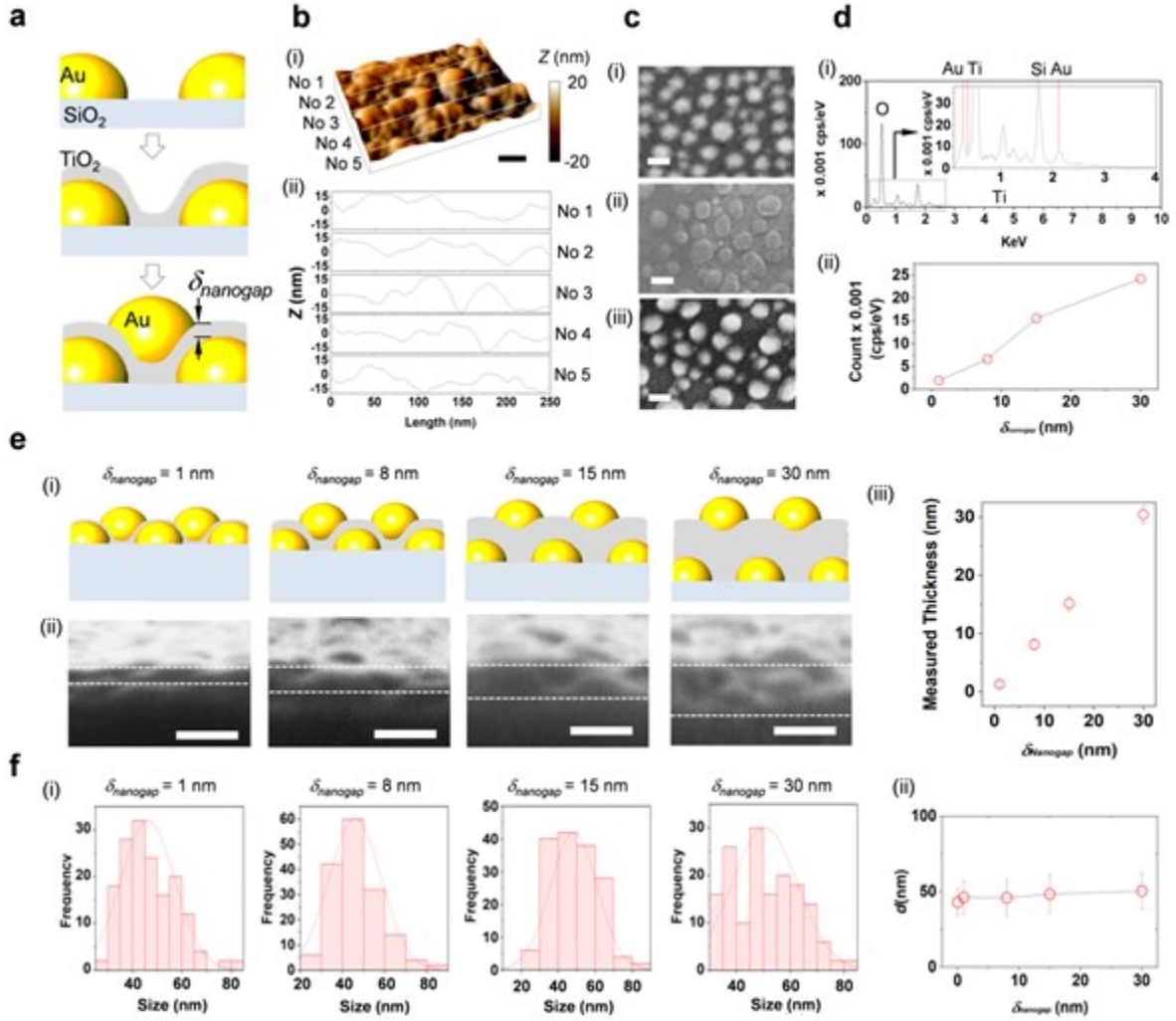

Figure 2. Characterization of multidimensional plasmonic nanogap bridged with a semiconductor layer in a large area substrate. (a) Schematic shows the fabrication procedure of PNA. (b) (i) AFM image and (ii) profiles of PNA ($\delta_{nanogap}$ = 8nm) (scale bar =50 nm) (c) SEM images of (i) AuNS array, (ii) TiO2/AuNS, and (ii) PNA ($\delta_{nanogap}$ = 8nm) (scale bar = 50 nm), and (iii) cross-section of the PNA as a function of $\delta_{nanogap}$ from 1 to 30 nm (scale bar = 50 nm). (d) (i) EDS spectrum of PNA ($\delta_{nanogap}$ = 8nm) and (ii) Ti counts as a function of $\delta_{nanogap}$ from 1 to 30 nm. (e) (i) Crossectional schematics, (ii) SEM images, and (iii) TiO_2 thickness of PNAs on glass substrates as a function of $\delta_{nanogap}$ from 1 to 30 nm. (f) Quantification of the morphology of PNAs: (i) average sizes and (ii) average diameter of AuNS as a function of $\delta_{nanogap}$ from 1 to 30 nm.

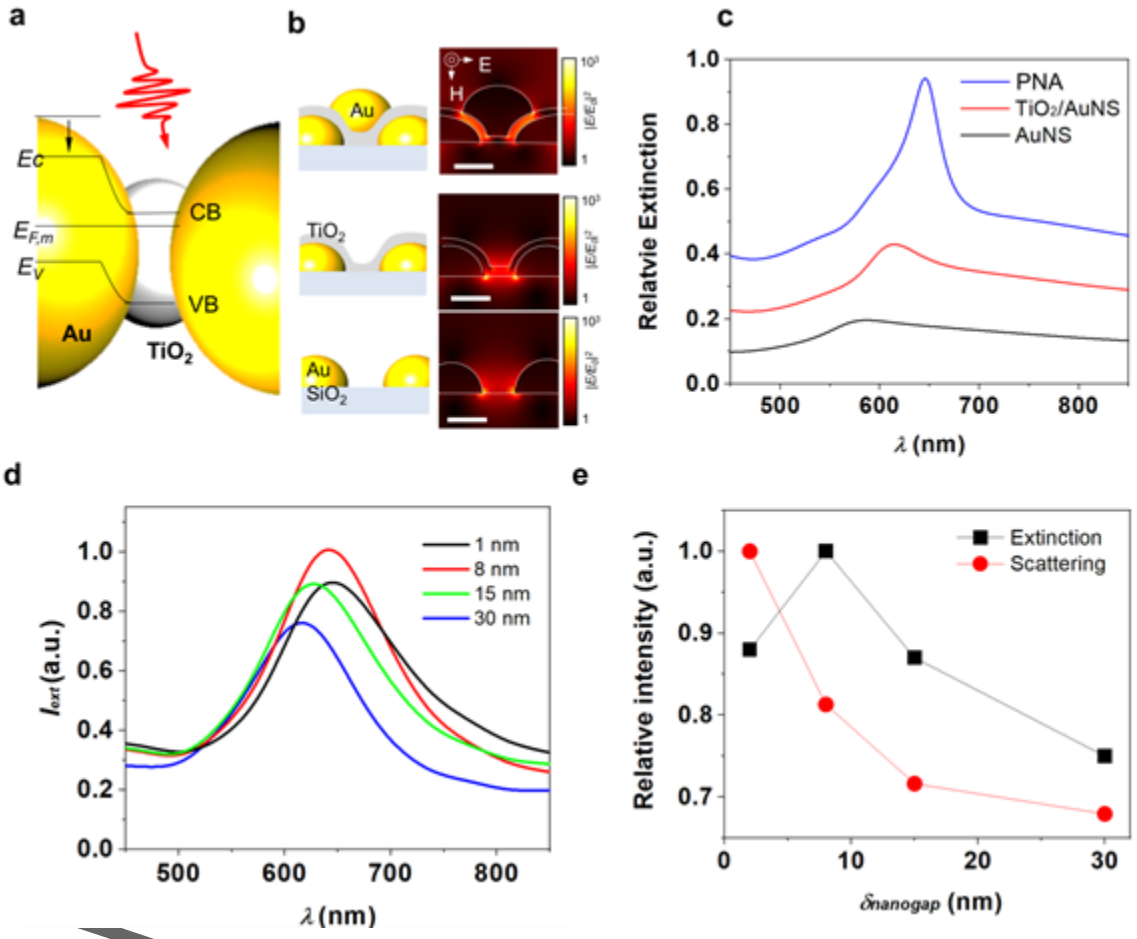

Figure 3. Optical properties of the multidimensional PNA. (a) Schematic of visible light focusing and charge separation in the PNA. The nanogap between AuNS layer of PNA leads to plasmonic coupling. The nanogap is filled with TiO_2 nanolayer. (b) Distribution of *E*- field around AuNS array, TiO_2/AuNS array, and PNA at λ = 650 nm (Scale bar = 40 nm). (c) Extinction spectra of AuNS, TiO_2/AuNS, and PNA. (d) Measured extinction spectrum as a function of $\delta_{nanogap}$ from 1 to 30 nm. (e) Comparison between absorption and scattering spectra as a function of $\delta_{nanogap}$ from 1 to 30 nm.

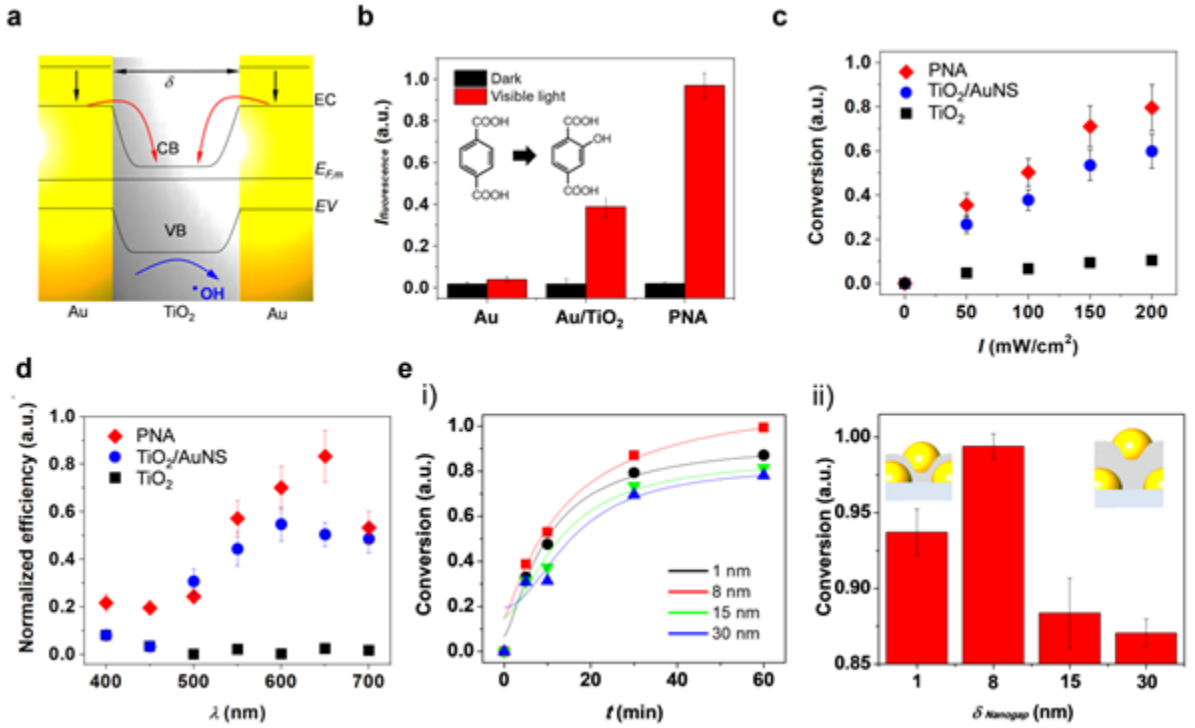

Figure 4 Visible light-induced photocatalytic performance in PNA. (a) A schematic diagram of charge separation and radical generation though the plasmonic nanogap of TiO_2 between AuNSs. (b) Quantification of OH radical generation; fluorescent intensity of sample the sample solutions prepared at pH 12.5 containing TA and 0.1 M Na_2SO_4 at I = 200 mW/cm^2 for 2 hrs. (c) Conversion of photocatalytic MB decomposition under visible illumination in the AuNS, TiO_2/AuNS, and PNA (δnanogap = 8 nm) nanostructures as a function of light intensity (I) from 0 (Dark) to 200 mW/cm^2 at Q = 2.0 mL/min. (d) Normalized efficiency of photocatalytic MB decomposition as a function of filter cut-off wavelength in the TiO_2, TiO_2/AuNS, and PNA (δnanogap = 8 nm) nanostructures at TiO_2, TiO_2/AuNS, and PNA at Q = 2.0 mL/min and I = 200 mW/cm^2. The normalized efficiency was estimated by normalization of the ratio between MB decomposition rate and number of photon absorption rate at each filter cut-off wavelength. Error bars represent the standard deviation of the systematic errors in the collection of spectrum data. (e) Nanogap effect on MB decomposition. i) Dynamics of photocatalytic performance as a function of δnanogap from 1 to 30 nm at Q = 2.0 mL/min and I = 200 mW/cm2. ii) Conversion of MB decomposition as a function of δnanogap from 1 to 30 nm at Q = 2.0 mL/min and I = 200 mW/cm^2.

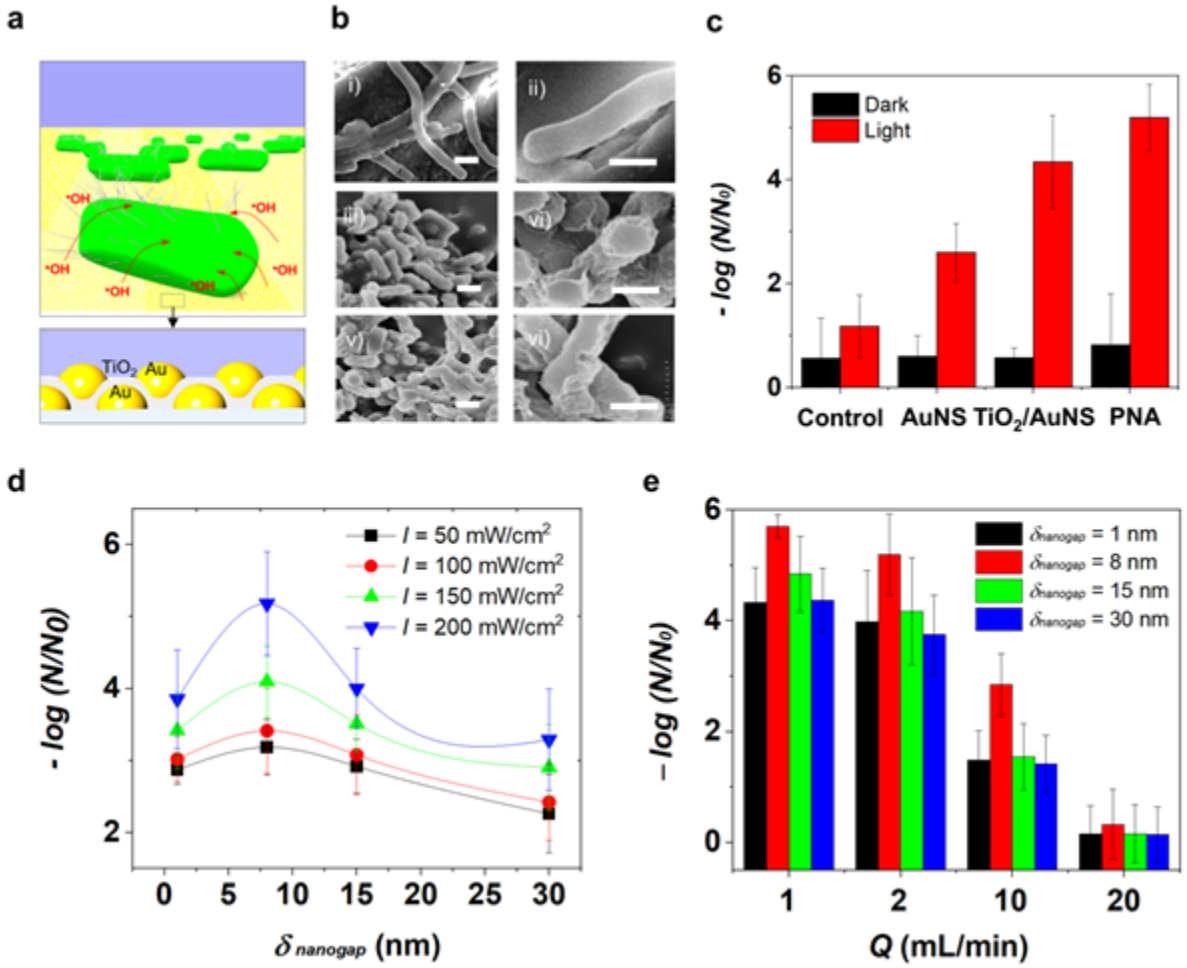

Figure 5. Visible light-induced water inactivation. (a) Schematic of interaction between the generated OH radicals from PNA and *E. coli* under visible light illumination. (b) SEM images of *E. coli* without any treatment i) –ii) and treated with AuNSs iii) –iv) and t PNA v)-vi) (scale = 0.5 um). (c) *E. coli* inactivation on control, AuNS, TiO_2/AuNS, and PNA with $\delta_{nanogap}$ = 8 nm at dark and light on (I = 200 mW/cm^2) after 60 mins. (d) *E. coli* inactivation as a function of $\delta_{nanogap}$ from 1 to 30 nm with varying I from 50 to 200 mW/cm^2 at Q = 2.0 mL/min under visible-light illumination. (e) *E. coli* inactivation performance as a function of Q from *1* to 20 mL/min at I = 200 mW/cm^2 with δnanogap varying from 1 to 30 nm.

DOI: 10.1002/ (smll.202006044R1)

The imbalance between light capture, charge transfer, and the required recycling steps has prohibited potential uses of plasmonic semiconductor structure for sustainable environmental process. This article presents a significantly improved visible-light-induced water treatment method that uses a plasmo-semiconductor nanogap bridge array (PNA).

Keyword: Interfacial antibacterial method, plasmo-semiconductor nanogap bridge, localized surface plasmon resonance (LSPR), bacteria, sustainable water treatment

*Emma Murphy,[a‡] Yunbo Liu,[b‡] Daniel Krueger,[c] Meghna Prasad,[a] Somin Eunice Lee,[*b,d] and Younggeun Park[*e]*

([*]Co-first authors are Emma Murphy[a‡] and Yunbo Liu,[b‡])

Title: **Visible-light induced Sustainable Water Treatment using Plasmo-semiconductor Nanogap bridge Array, PNA**

ToC figure ((Please choose one size: 55 mm broad × 50 mm high **or** 110 mm broad × 20 mm high. Please do not use any other dimensions))